This is the peer-reviewed, final accepted version for American Mineralogist, published by the Mineralogical Society of America.
The published version is subject to change. Cite as Authors (Year) Title. American Mineralogist, in press.
DOI: https://doi.org/10.2138/am-2022-8442. http://www.minsocam.org/

Revision 2

Microbially Induced Clay Weathering: Smectite-to-Kaolinite Transformation

Xiaoxue Yang[1#], Yanzhang Li[1#], Yan Li[1], Anhuai Lu[1*], Hailiang Dong[2,3], Song Jin[4], Hongrui Ding[1]

[1]Beijing Key Laboratory of Mineral Environmental Function, and The Key Laboratory of Orogenic Belts and Crustal Evolution, School of Earth and Space Sciences, Peking University, Beijing 100871, PR China

[2]Center for Geomicrobiology and Biogeochemistry Research, State Key Laboratory of Biogeology and Environmental Geology, China University of Geosciences, Beijing 100083, P.R. China

[3]Department of Geology and Environmental Earth Science, Miami University, Oxford, Ohio 45056, United States

[4]Advanced Environmental Technologies LLC, 4025 Automation Way, Unit F4, Fort Collins, CO 80525, USA; and Department of Civil and Architectural Engineering, University of Wyoming, Laramie, WY 82071, USA

[*]Corresponding author: Anhuai Lu, Email: ahlu@pku.edu.cn.

[#]These authors contribute equally.

Abstract

Microbially induced formation and transformation of clay minerals are known to be ubiquitous in nature. This work investigated the smectite-to-kaolinite transformation by *Bacillus mucilaginosus*, a kind of silicate-weathering bacterium. Results showed that the microbe-smectite system doubled protein production compared with the abiotic controls, and enhanced dissolved 1.6% of total Si and 0.9% of total Al from smectite after the 25 days experiment. The formation of kaolinite was verified through its distinguished $d_{(001)}$-spacing of 0.710 nm revealed by synchrotron radiation X-ray diffraction (SR-XRD) and high-resolution transmission electron microscope (HR-TEM). HR-TEM analysis indicated some mixed layers of smectite and kaolinite appeared in the form of a superlattice structure. Moreover, the compositional and morphological changes of the solids suggested the emergence of kaolinite was associated with the formation of amorphous SiO_2 and fragmented clay particles with lower Si/Al ratio and exposed crystal edge. Based on the detection of -C=O species on smectite surface, and the decrease of pH from 8.5 to 6.5, we inferred the organic ligands secreted by *Bacillus mucilaginosus* complexed with cations especially for Si, which stripped the tetrahedral sheets and promoted the kaolinization of smectite. To our knowledge, this is the first report of microbially induced smectite-to-kaolinite transformation under ambient conditions in a highly-efficient way. This work could shed light on a novel pathway of microbe-promoted weathering of smectite to kaolinite at the Earth surface conditions. Such a robust and efficient transformation from expansive smectite to non-expansive clays as kaolinite could be of great potential in

enhancing oil recovery in reservoirs.

Key words: Smectite-to-kaolinite transformation, Clay minerals, *Bacillus mucilaginosus*, superlattice structure, microorganism

Introduction

Clay minerals and microorganisms are two of the most essential and associative components on Earth (Dong et al., 2009; Mueller, 2015; Cuadros, 2017; Li et al., 2019). Microorganisms (e.g., bacteria and fungi) can facilitate the formation and transformation of clay minerals through nucleation (Konhauser et al., 1993), biomineralization (Kawano and Tomita, 2001), dissolution (Banfield et al., 1999), alteration (Dudek et al., 2006), etc. In reverse, redox and decomposition of clay minerals can either provide electron energy or elemental nutrients for microbial growth (Kim et al., 2014; Cuadros, 2017; Li et al., 2019).

The mutual transformation of kaolinite, smectite and illite, which are three clay minerals with the most abundant and reactive mixed layers in soil, have been experimentally demonstrated under different biotic and abiotic conditions (Bergaya, and Lagaly, 2006; Dong et al., 2009; Cuadros et al., 2017). In particular, the interconversion of 2:1 type clay minerals, i.e. smectite and illite, has been reported to occur by the catalysis of microorganisms under ambient conditions, in which the microbial redox of Fe(III)/Fe(II) pair was the key to regulate interlayer cations and final mineral phases (Manceau et al., 2000; Dong et al., 2009; Shelobolina et al., 2012; Kim et al., 2014; Zhao et al., 2017). In

comparison, the transformation of 1:1 type clay minerals such as kaolinite to 2:1 type clays of smectite/illite is more difficult due to the requirement of other well-matched tetrahedral sheets. Even so, the illitization or smectitization of kaolinite has been demonstrated to occur through the simultaneous uptake of Si, Fe and Mg, bio-reduction of Fe and fixation of K, which requires intricate dissolution and precipitation (Andrade et al., 2014; Cuadros et al., 2017).

However, the opposite process of microbial kaolinization of smectite or illite, has received less attention. In geological settings, the kaolinization of smectite is an important proxy of paleoclimate change; and kaolinite is generally a product of highly hydrolytic weathering in warm humid climates (Altschuler et al., 1963; Karathanasis and Hajek, 1983; Robert et al., 1992; Amouric and Olives, 1998; Dudek et al., 2006; Ryan and Huertas, 2013; Zhang et al., 2016). According to these previous reports, the driving force for the transformation of smectite to kaolinite has only been attributed to inorganic processes, in which tetrahedral sheets of initial smectite are stripped or regrouped with octahedral sheets to form kaolinite. Zhao et al. (2017) reported the transformation of illite to smectite and eventually kaolinite by an anaerobic Fe(II)-oxidizing bacteria over 24 months. In this case, the Fe(II) oxidation was firstly accompanied with an exchange of K^+ in illite by Mg^{2+} and then the formation of smectite. The following dissolution of tetrahedral sheets in illite and smectite under long-term bacterial incubation helped convert into kaolinite by mainly aqueous dissolution/crystallization mechanisms. This new microbial kaolinization process seems less efficient due to its indirect correlation with the Fe(II)-oxidizing function of

anaerobic microorganisms.

In this study, the stripping of the tetrahedral sheets of smectite was successfully achieved by a common soil bacterium *Bacillus mucilaginosus* (*B. mucilaginosus*), with a super ability of weathering silicate minerals (Malinovskaya et al., 1990; Basak and Biswas, 2009; Mo and Lian, 2011; Lv et al., 2019). Mineralogical characterizations of X-ray diffraction (XRD), high-resolution transmission electron microscope (HR-TEM), scanning electron microscope (SEM), X-ray photoelectron spectroscopy (XPS), and Fourier transform (infrared spectroscopy) FT-IR analysis, comprehensively indicated the kaolinization of smectite by the bacteria. The aim of this work is to reveal a novel efficient pathway for smectite-to-kaolinite transformation through microbial mechanisms.

Materials and methods

Purification of smectite

Natural smectite samples from Liaoning Province, China, were dried at 80°C for 2 h before being ground and passed through a 200-mesh sieve. Powder samples with particle size less than 74 μm were taken and stored for subsequent experiments. The specific steps of purification are as follows. Firstly, 10 g of the above-mentioned powders were mixed with 200 mL high pure water (18 MΩ·cm) and thoroughly stirred to form a suspension, followed by the separate addition of 0.12 mL $NaHCO_3$ (1 mol/L) and 0.02 g $Na_2S_2O_3$. This suspension was subjected to continual stirring and intensive mixing before being heated in a water bath at 90°C for 5 mins. Next, carbonate mineral impurities were removed by pipetting diluted HCl (0.2 mol/L) into the solution until its pH decreased to ~3.5. Finally, the obtained suspension was filtered by a vacuum pump and washed repeatedly 5-6 times. XRD was used to demonstrate its high purity of the solid sample, shown in our previous work (Yang et al., 2016). The structural formula of pure smectite, as $Na_{0.58}Ca_{0.04}(Al_{1.17}Mg_{0.46}Fe_{0.38})(Si_{3.78}Al_{0.22})O_{10}(OH)_2$, has been determined by electron microprobe analysis (data not shown).

Identification of solid samples

Powder XRD patterns based on synchrotron radiation technology were collected at BL14B1 beamline in Shanghai Synchrotron Radiation Facility (SSRF). XRD data were recorded using a six-circle Huber 5021 diffractometer system equipped with MYTHEN 1K

detector (Gao et al., 2016). X-ray energy was identified as 10 eV (i.e., corresponding wavelength as 0.12398 nm) according to LaB_6 standard. Powder samples were loaded into commercial glass capillaries perpendicular to the beam (0.5 mm in diameter and wall thickness ~ 0.01 mm) with a spot size of 300×300 μm.

Morphology of samples was observed in a Nova nano SEM 230 (FEI, USA) at 10 kV and pressure of 45 Pa. A JEOL2100F TEM (JEOL, Japan) was used at 200 kV equipped with an energy-dispersive X-ray (EDX) analyzer. Before TEM measurement, samples were embedded in pure LR-white resin for 1 h at 40°C and then for 24 h at 60°C before a micro area (100×100 μm) with thickness of 70-90 nm was sectioned by focused ion beam (FIB) Zeiss Auriga Compact system (Zeiss, Germany). The TEM lattice fringe images of clay minerals are hard to obtain because the electron beam often cause damage to the structure. Therefore, images of areas displaying lattice fringe were captured with minimum focusing near interested regions, without any adjustment to increase the resolution. Digital Micrograph software (version 3.9) was used for picture processing.

XPS was carried out by using a PHI Quantera II instrument (Ulvac-Phi, Japan) attached with an Al Kα source (1486.6 eV). The C 1s peak of 284.8 eV was used as an internal reference for absolute binding energy. The curve-fitting software was indicated above. FT-IR was conducted using a NICOLET iN10MX FT-IR spectrometer (Thermo Fisher Scientific, USA). The spectra were collected in transmission mode with a resolution of 4 cm^{-1} over the 500-4000 cm^{-1} spectral range.

Bacterial culture

The culture medium for *B. mucilaginosus* strain, which was applied both in bacterial culture and subsequent experiments with smectite, contained 1.0 g/L of yeast extract, 5.0 g/L of sucrose, 0.5 g/L of $MgSO_4 \cdot 7H_2O$, 0.2 g/L of K_2HPO_4, 5 mg/L of $FeCl_3 \cdot 6H_2O$, and 10 mg/L of $CaCl_2$ in high pure water (18 MΩ·cm). The culture medium was adjusted to pH as 7.20 with 0.1 mol/L HCl and was autoclaved at 120°C for 20 minutes for sterilization. Cell suspensions were prepared by adding 1 mL of seed culture to 100 mL of culture medium, which were then cultured in an incubator (35°C, 150 rpm) for 48 h until the late log phase.

Interaction of smectite and B. mucilaginosus

A series of batch experiments were performed at aerobic conditions (25°C, 0.1 MPa) with three systems and triplicates. For the system with living cells and smectite (denoted as "SBM"), 0.5 g purified smectite powders was added to 50 mL medium and then sterilized, which was added into 40 mL of above activated cell suspension and 10 mL of sterilized fresh culture medium. The system with heat-inactivated cells and smectite (denoted as "SA") was similar to the SBM system, with the exception that 40 mL of cell suspension was autoclaved at 120°C for 20 minutes and repeated three times in advance. The third system was abiotic with no cells, (denoted as "SC"): 0.5 g purified smectite powders was directly mixed with 100 mL of sterilized culture medium. All flasks contained 100 mL suspension and were cultured in an oscillating incubator (35°C, 150 rpm) for 25

days.

Every five days, 3.5 mL suspension was extracted from each system for the measurement of protein, pH, and dissolved cations. The commercial Bradford protein assay (Zor and Selinger, 1996) was used, which can react with residues at amino acids and become the chromophore. Briefly, unfiltered aliquot (200 μL) was boiled for 10 minutes after the addition of 0.1 mL NaOH (0.2 mol/L) and 1.7 mL saline (0.9%). The supernatant (1.6 mL) was added to 0.4 mL Bradford protein assay after centrifugation before the absorbance was detected at 590 nm and 450 nm due to the binding of Coomassie brilliant blue G-250 (CBBG) to proteins. The ratio of the absorbances, 590 nm over 450 nm, is strictly linear with protein concentration, which was monitored by UV-Vis spectrophotometer (Thermo Fisher Scientific, USA). The standard curve (R^2=0.999) was built in advance using protein standard solution (BSA) (1.6 mL) and Bradford protein assay (0.4 mL). Simultaneously, 1.5 mL extracted suspension was filtered and 1 mL supernatant was diluted to 10 mL with 2% v/v HNO_3. The concentration of dissolved Si and Al was quantified by inductively coupled plasma optical emission spectroscopy (ICP-OES) (Spectro, Germany). The rest of the extracted suspension was monitored for pH. Solid products were collected on day 5, 10, and 25, by the process of first separation from 5 mL suspension after centrifugation, and then being cleaned with high pure water (18 MΩ·cm) by three times before being dried at 60°C for 24 h.

Results

Bacterial growth coupled with chemical changes in the solution

The protein concentration from living cells and their exudates, which was used as the indicator of living-cell metabolic activity, remarkably enhanced from the initial 27.9 mg/L to 75.3 mg/L within 15 days in the presence of both smectite and bacteria (SBM group) (Fig. 1a). Consistently, a sharp decrease of pH from 8.53 to 6.65 on the fifth day was observed, which indicated the acidic metabolites were produced by the living bacteria during their growth. By contrast, both the protein and pH in control experiment with heat-inactivated cells (SA group) kept almost constant during the whole reaction time, suggesting no effective interactions occurred between the inactive cells and smectite. As expected, the pH of the abiotic control (SC group) also remained unchanged. Therefore, the growth of *B. mucilaginosus* in SBM group increased the acidity of the system.

The release of Si and Al from smectite was observed during the reaction time, while other cations were below the detectable levels (data not shown). In the system with *B. mucilaginosus* and smectite, the concentration of Si and Al dramatically increased within 5 days and peaked at 43.54 mg/L and 9.06 mg/L, respectively. The peak values account for 1.6% and 0.9% of the total Si and Al in smectite, respectively, so the releasing rate of Si was slightly higher than that of Al. The accumulation of Si in solution decreased after the fifth day and dropped to 16.52 mg/L after 25 days while Al was almost reduced to zero. The decrease of Si and Al in the solution could be ascribed to the electrostatic adsorption by electronegative bacterial cells or precipitation as (oxyhydr) oxides at neutral conditions (pH of 6-7). The concentration of dissolved Si and Al showed very slight fluctuation around

their initial value in the other two controls; this distinct contrast with the living-cell system yielded similar results for pH and protein in Fig. 1a. The sum of evidence points to a noteworthy interaction between microbes and smectite.

Morphology and element changes of smectite

The reaction of smectite with heat-inactivated cells did not present any changes in terms of morphology, which remained a layered and tight structure like the raw material (Fig. 2a). After continuous interaction with *B. mucilaginosus* for 25 days, smectite became fragmented and its thin layers rolled up (Fig. 2b). It is found that some bacteria (white arrow in Fig. 2b) lay in tight contact with the mineral, and there is a thick biofilm in between. These features are similar to reported observations for other clay minerals in terms of microbial activities (Dong et al., 2003). Particularly, there were considerable particles with a uniform size of 20-30 nanometers found on the unsmooth surface of smectite after a 25-day interaction with microorganisms (Fig. 2c). These particles are mainly composed of Si and O, whose selected area electron diffraction (SAED) pattern present diffuse rings. These nanoparticles can possibly be amorphous SiO_2 precipitated from released Si, according to the consumption of dissolved Si (Fig. 1b).

XPS was used to detect the change of Si, Al, Mg, Ca, and Fe in the final solid products obtained in the living-cell system and abiotic control (Fig. 3). Compared with the abiotic control, the peak area of Si decreased after the interaction of smectite and *B. mucilaginosus*. The disappearance of Si in solid products, as shown in Fig. 1b, can be ascribed to its

dissolution into the solution. However, differently from Si, the concentration of other cations (Al, Mg, Ca, Fe) had no significant decrease; in fact, they slightly increased in the detectable region of XPS. Compared with the blank group without *B. mucilaginosus*, the residual solid after the reaction with that microbe has lower Si/Al, Si/Mg, Si/Ca and Si/Fe (Table 1). This suggests that Si is able to be more easily released from smectite than other cations under the influence of microbes in the experiment of 25 days.

Table 1 XPS peak area ratio of detected atoms on smectite in living cells system (SBM) and the blank group (SC).

Peak area ratio	Si/Al	Si/Mg	Si/Ca	Si/Fe
SC	7.59	42.09	4.32	2.29
SBM	6.51	37.12	3.55	1.98

New phase identification

Solid product phases extracted in three experiment systems on 5, 10, and 25 days were examined by SR-XRD (Fig. 4). There were no observable changes in the XRD patterns for the three samples from the abiotic control system (the bottom panel of Fig. 4), whose phase pointed to pure randomly-oriented smectite with three dominant diffraction peaks of (001) (d=1.590 nm), (02,11) (0.451 nm), and (13,20) (0.256 nm) (Ryan and Huertas, 2009). The control system with heat-inactivated cells also presented unchanged structure of smectite within 25 days (the middle panel of Fig. 4). By contrast, change in samples was more

noticeable in the living-cell system. On the tenth day, the peak position of (001) plane shifted marginally to a lower angle, indicating the swelling of smectite along the stacking direction of layers. In addition, both intensities of peaks belonging to (02,11) and (13,20) were dramatically enhanced and tailed off towards lower d-values. Notably, a new plane with a spacing of 2.230 nm emerged in the 10-day product; its intensity became stronger after reacting with the microbe for 25 days (the upper panel of Fig. 4). The most striking feature in the final sample was the emergence of the other diffraction peak with *d*-spacing of 0.710 nm. In this case, the characteristic *d*-spacing (0.710 nm) can be assigned to the (001) plane of kaolinite instead of serpentine due to the absence of hydrothermal or metamorphic processes.

The emergence of kaolinite is the direct indicator that smectite has been partially dissolved by *B. mucilaginosus*. Note that the other new *d*-spacing (2.230) is equal to the sum of 1.490 nm from the initial smectite and 0.710 nm from the produced kaolinite. As a result, the new unknown species might have a superlattice structure. In other words, the newly generated kaolinite could not be from the simple reprecipitation of dissolved Si and Al, but rather an on-site product that is still trapped in the lattice of smectite. The superlattice structure is common in kaolinitic smectite during abiotic progressive kaolinization (Altschuler et al.,1967; Amouric and Olives, 1998).

The transmission electron microscopy (TEM) lattice fringe images of smectite reacting with heat-inactivated bacteria showed a main d-spacing of ~1.21 nm, which was assigned

to the typical (001) plane of smectite (Fig. 5a-c). XRD yielded a marginally smaller value, which may be attributed to the dehydration of hydrous smectite under the exposure of the electronic beam. The smectite was subjected to different levels of alteration when reacting with living *B. mucilaginosus;* some smaller (001) planes (d=0.728 nm) accounted for a small fraction of an initial smectite particle (Fig. 5d-e). The region with the produced new phase had higher Al/Si ratio (Fig. f) compared with the unchanged system (Fig. 5c). According to the XRD results, the new phase embedded into smectite can be assigned to kaolinite, proving a kaolinization in smectite caused by bacteria. Wider planes with *d*-spacing of 1.943 nm also behaved similarly with kaolinite characteristics (Fig. 5g-h). Consistent with the XRD results, this wide *d*-spacing was the sum of 1.213 nm from the initial smectite and 0.730 nm from the newly-formed kaolinite. This can reflect the transition from smectite layers to super-lattice structure of smectite-kaolinite layers (Altschuler et al., 1963). A higher Al/Si ratio was also observed in such a region with a super-lattice structure (Fig. 5i), reflecting the greater loss of Si than Al. Referring to the stacking defect model of kaolinite (Kogure and Inoue, 2005), a smectite-kaolinite mixed-layer with super-lattice structure and corresponding HRTEM image is shown in Fig. 6, which indicated a close spatial relationship between smectite and kaolinite.

Organic acid on solid products

FTIR spectra show that all solid samples have dual dominant peaks at 1050 and 3400 cm^{-1} (Fig. 7), corresponding to Si-O stretching and O-H stretching vibrations, respectively.

Notably, a new absorption signal emerged at 1723 cm^{-1} after 5 days of experiment in the living-cell system (Fig. 7a) (Ulagappan and Frei, 2000). This new peak was attributed to the antisymmetric stretching vibration of -C=O bonds in carboxyl groups. In abiotic control, the peak was absent (Fig. 7b). Some carbon species in C 1s core-level XPS at 284.4, 286.3, and 288.9 eV were ascribed to-C-C, -C-O, and -C=O, respectively (McCafferty and Wightman, 1998). Based on these assignments, the concentration of -C-O and -C=O species on solid products in living-cell system was enhanced almost 10% over 25 days compared with the abiotic control (Fig. 7c and 7d). Considering the organic carbon contamination in abiotic control occurred from atmospheric deposition, the enhancement of -C-O and -C=O species in SBM group was caused by the actions of *B. mucilaginosus*. Both FTIR and XPS spectra suggested the carboxyl groups of organic acid in metabolites were found on the solid products.

Discussion

Release of Si from smectite by B. mucilaginosus

B. mucilaginosus is a common soil bacterium (Liu et al., 2006; Basak and Biswas, 2009; Mo and Lian, 2011; Yang et al., 2016) with silicate mineral weathering ability. It can secrete organic acids and polysaccharides and form ligands with cations on mineral surfaces, thus resulting in the dissolution of silicates (Banfield et al., 1999; Liu et al., 2006; Basak and Biswas, 2009; Mo and Lian, 2011). Our results indicate that the formation of organic acids during the microbe-smectite interaction (Fig. 7), significantly deceased the

pH from 8.53 to 5.94 within 25 days (Fig. 1), which could be oxalic, citric or lactic acids according to one previous research (Liu et al., 2006). And it was found that the microbe-smectite system dissolved 1.6% of total Si and 0.9% of total Al after the 25 days experiment (Fig. 1b). The faster releasing rate of tetrahedral Si (almost double) than that of Al, as well as the observation of produced SiO_2 nanoparticles (Fig. 2c) confirmed the bacterial activity mainly resulted in the disassembling of the Si-O tetrahedral sheets. The dissolution of Al could be come from substituted Al for Si and some destroyed octahedral sheets. Consistently, the residual cations on the surface of minerals showed the octahedrally occupied cations like Al, Mg, and Fe slightly increased whereas Si decreased (Fig. 3 and Table 1), also indicating the removing of Si sheets from the structure and the resulting exposure of octahedral sheets. Based on morphology observations, after interacting with microbes, smectite became fragmented and its initial thin layers rolled up (Fig. 2b). The broken of smectite can result in more exposure of cations, thus promoting the complexing of organic acids with surface exposed metal cations as Al, Mg, and Fe. Notably, the edge surfaces characterized by broken bonds were much more active than the basal surfaces (White and Zelazny, 1988; Bickmore et al., 2001), implying that the deconstruction of smectite lattice could start from its crystal edges. Moreover, there was no obvious expansion of smectite interlayer after its reaction with microbes, based on XRD patterns (Fig. 4), indicating that especially larger organic molecules have not entered the interlayer yet. Although there are still some possibilities that small organics could enter the interlayer, their effect on the dissolution of Si must be less remarkable than those organics at layer

edge sites. Therefore, organic acids could react less with cations at basal surfaces, but can mainly attack cations at layer edge sites through complexation reactions.

Note that the Mg-O and Al-O bonds are much weaker than Si-O bond (Keller, 1954), so the main dissolution of Si rather than Mg, Fe, Ca or Al indicates the complexity of the involved mechanism. According to previous works about the silicate dissolution in organic acids (Welch and Ullman, 1996), it was found that the dissolution rate is strongly dependent on the nature of the ligand. In particular, oxalate has a greater impact on dissolution rates of the Ca,Al-rich silicates, while catechol can form strong complexes with both Al and Si. It suggests some organics could specifically break stronger Si-O bonds instead of Mg, Fe or Ca. More importantly, in the absence of any ligands, the rate of Si dissolution from silicate minerals in acid condition is generally faster than that of Al (Wollast, 1967; Chin and Mills, 1991). It could be attributed to the first hydrolyzation of the tetrahedral layer silica units to dissolved silicic acid (H_4SiO_4), which even can be adsorbed back to Al sites and thus retard the dissolution of Al (Jepson et al., 1996). In our study, therefore, the faster dissolution of Si than that of Al, Ca, Mg, Fe could be interpreted by the production of specific organics as effective ligands and/or the proton-assisted formation of dissolved silicic acid. This complexation weakened the connection of O atom in the surface tetrahedral sheets with the metal in the inner octahedral sheets, ultimately causing the detachment of the surface tetrahedral Si-O sheets. Previous work on the transformation of smectite to kaolinite via hydrothermal treatment also pointed out tetrahedral sheets were more easily to be stripped off; conversely, octahedral sheets interior to tetrahedral sheets

were more likely to be preserved (Ryan and Huertas, 2013).

Smectite to kaolinite transformation

The secondary mineral derived from the transformation of smectite, as identified by XRD (Fig. 4) and TEM (Fig. 5), was kaolinite with a tetrahedral sheet and an octahedral sheet in its unit cell. Previous researches about the abiogenic transformation from smectite to kaolinite mainly pointed to two models. One proposes that tetrahedral sheets were stripped off at crystal edges and kaolinite-like patches formed, accompanied with the collapse of interlayers to ~7 Å. This produced tabular kaolinite when kaolinite-like patches were large enough (Altschuler et al., 1963; Amouric and Olives, 1998; Dudek et al., 2006). Alternatively, the recrystallization from dissolved Al with Si or new Al-rich octahedral sheets and up-down inversed tetrahedrons can directly produce kaolinite (Karathanasis and Hajek, 1983) (Ryan and Huertas, 2013). As a result, it's reasonable to link the formation of kaolinite to the stripping of tetrahedral sheet from smectite or the possible recrystallization of dissolved Al with Si. In our case, due to the nearly double dissolved rate of Si than Al, kaolinite is more than likely produced by the faster loss of tetrahedral sheets.

Notably, when the produced kaolinite layers were not continuous along the c crystallographic axis but consistent within other layers, a superlattice structure can appear. For example, an alternate mixed layer with one smectite layer and one kaolin layer created a ~2.2 nm superlattice (Fig. 4-6 and 8). The superlattice of kaolinite-smectite revealed that the alteration of smectite to kaolinite was a structural transformation and an incomplete

progress (Altschuler et al., 1963). According to TEM images (Fig. 5 and 6), both formed kaolinite and superlattice layers were tightly distributed at the edge of smectite particles, not their inner parts. All of these layers were quasi-continuous along the c crystallographic axis and existed within the same particles. As a result, it was confirmed that the formation of kaolinite from smectite was attributed to the stripping of tetrahedral sheets (Fig. 8). To our knowledge, this represents the first study of smectite-kaolinite transformation by microorganisms with a high efficiency. Essential elements such as Na and Ca, discharged from the interlayer during the smectite-to-kaolinite transformation due to the consequent deconstruction of interlayer spaces, can enter the cells of *B. mucilaginosus* and facilitate their growth (Xiao et al., 2014). The fast production of proteins in the system of smectite and living *B. mucilaginosus* (Fig. 1) proved the destruction of smectite promoted the bacterial growth and this might be an energy-gaining process. Organic acids and other possible products (like polysaccharides) as critical extracellular polymeric substance destabilized the smectite lattice, reflecting a common and artful interaction between microorganisms and natural minerals.

These results together suggested the interaction between *B. mucilaginosus* and smectite probably occurred as follows (schematically showed in Fig. 8). Firstly, the organic acids produced by the bacteria as ligands bonded with cations at edge surfaces, weakening the metal-oxygen bonds. Next, alternative or both outside tetrahedral sheets were stripped off from the stable interior octahedral sheets. Finally, Si was released into the solution, accompanied by the formation of fragmented clay particles containing mixed layers of

initial smectite and produced kaolinite. In this work, long-term experiments longer than 25 days are absent, thus whether the smectite-to-kaolinite transformation could achieve equilibrium or octahedral sheets could be further decomposed are worth more future work.

Implications

The silicate-weathering bacterium used in this work, which is widespread in soil, can directly attacked Si-O bonds in smectite. The conversion of smectite to kaolinite is thus more direct, oriented and highly-efficient than the abiotic processes. Notably, the capabilities of water and cations in interlayer space of smectite are so outstanding that smectite-to-kaolinite transformation by microorganisms can probably facilitate the weathering of smectite-dominated soil, which gives rise to the destruction of interlayer space and the consequent release of cations. The new discovery of smectite-to-kaolinite transformation under the influence of microorganisms thus helps to bring knowledge and light about the formation, weathering, and diagenesis of clay minerals.

Such a process also has some promising applications. For example, in some petroleum reservoirs with high content of smectite, the swelling of smectite often occurs in oil recovery using waterflooding methods, which seriously blocks pore throats and causes decreasing permeability as well as oil recovery. Microbial induced kaolinization of smectite provides an on-site and high-performance strategy of transforming expansive smectite to non-expansive kaolinite, thus to reduce water sensitivity of reservoirs and enhance oil recovery efficiency. Notably, widespread silicate-weathering bacteria can even

survive and play roles in destructing silicate minerals in high-temperature environments like hot springs (>90°C) (Rajawat et al., 2020), and *B. mucilaginosus* used this work has the limiting survival temperature over 50°C (Biswas and Basak, 2014). The proposed strategy, therefore, not only functions at surface conditions, but could even work at deep oil reservoirs with moderate temperature.

Acknowledgments: This work was supported by the National Natural Science Foundation of China (Grant No. 41820104003 and 41522201).

References:

Altschuler Z.S., Dwornik E.J. and Kramer H. (1963) Transformation of montmorillonite to kaolinite during weathering. Science, 141(3576), 148-152.

Amouric M. and Olives J. (1998) Transformation mechanisms and interstratification in conversion of smectite to kaolinite: an HRTEM study. Clays and Clay Minerals, 46, 521-527.

Andrade, G.R.P., de Azevedo, A.C., Cuadros, J., Souza Jr, V.S., Correia Furquim, S.A., Kiyohara, P.K., and Vidal-Torrado, P. (2014) Transformation of Kaolinite into Smectite and Iron-Illite in Brazilian Mangrove Soils. Soil Science Society of America Journal, 78(2), 655-672.

Banfield, J.F., Barker, W.W., Welch, S.A., and Taunton, A. (1999) Biological impact on mineral dissolution: application of the lichen model to understanding mineral weathering in the rhizosphere. Proceedings of the National Academy of Sciences, 96(7), 3404-3411.

Basak, B.B., and Biswas, D.R. (2009) Influence of potassium solubilizing microorganism (Bacillus mucilaginosus) and waste mica on potassium uptake dynamics by sudan grass (Sorghum vulgare Pers.) grown under two Alfisols. Plant and Soil, 317(1), 235-255.

Bergaya, F., and Lagaly, G. (2006) Handbook of clay science. Elsevier.

Bickmore, B.R., Bosbach, D., Hochella Jr, M.F., Charlet, L., and Rufe, E. (2001) In situ atomic force microscopy study of hectorite and nontronite dissolution: Implications

for phyllosilicate edge surface structures and dissolution mechanisms. American Mineralogist, 86(4), 411-423.

Biswas, D. R., & Basak, B. B. (2014). Mobilization of potassium from waste mica by potassium-solubilizing bacteria (Bacillus mucilaginosus) as influenced by temperature andincubation period under in vitro laboratory conditions. Agrochimica, 58(4):309-320.

Chin, P. K. F., & Mills, G. L. (1991). Kinetics and mechanisms of kaolinite dissolution: effects of organic ligands. Chemical Geology, 90(3-4), 307-317.

Cuadros, J. (2017) Clay minerals interaction with microorganisms: a review. Clay Minerals, 52(2), 235-261.

Cuadros, J., Andrade, G., Ferreira, T.O., de Moya Partiti, C.S., Cohen, R., and Vidal-Torrado, P. (2017) The mangrove reactor: fast clay transformation and potassium sink. Applied Clay Science, 140, 50-58.

Dong H.L., Kostka J.E., and Kim J.W. (2003) Microscopic evidence for microbial dissolution of smectite. Clays and Clay Minerals, 51(5), 502–512.

Dong, H., Jaisi, D.P., Kim, J., and Zhang, G. (2009) Microbe-clay mineral interactions. American Mineralogist, 94(11-12), 1505-1519.

Dudek, T., Cuadros, J., and Fiore, S. (2006) Interstratified kaolinite-smectite: Nature of the layers and mechanism of smectite kaolinization. American Mineralogist, 91(1), 159-170.

Gao M., Gu Y., Li L., Gong Z., Gao X. and Wen W. (2016) Facile usage of a MYTHEN

1K with a Huber 5021 diffractometer and angular calibration in operando experiments. Journal of Applied Crystallography, 49, 1182-1189.

Jepson, W. B., Jeffs, D. G., & Ferris, A. P. (1976). The adsorption of silica on gibbsite and its relevance to the kaolinite surface. Journal of Colloid and Interface Science, 55(2), 454-461.

Karathanasis, A.D., and Hajek, B.F. (1983) Transformation of smectite to kaolinite in naturally acid soil systems: Structural and thermodynamic considerations. Soil Science Society of America Journal, 47(1), 158-163.

Kawano, M., and Tomita, K. (2001) Microbial biomineralization in weathered volcanic ash deposit and formation of biogenic minerals by experimental incubation. American Mineralogist, 86(4), 400-410.

Keller, W. D. (1954). The bonding energies of some silicate minerals. American Mineralogist, 39(9-10), 783-793.

Kim, J., Dong, H., Seabaugh, J., Newell, S.W., and Eberl, D.D. (2004) Role of microbes in the smectite-to-illite reaction. Science, 303(5659), 830-832.

Kogure T. and Inoue A. (2005) Stacking defects and long-period polytypes in kaolin minerals from a hydrothermal deposit. European Journal of Mineralogy, 17, 465-474.

Konhauser, K. O., Fyfe, W.S., Ferris, F.G., and Beveridge, T.J. (1993) Metal sorption and mineral precipitation by bacteria in two Amazonian river systems: Rio Solimoes and Rio Negro, Brazil. Geology, 21(12), 1103-1106.

Li, G.L., Zhou, C.H., Fiore, S., and Yu, W.H. (2019) Interactions between microorganisms

and clay minerals: New insights and broader applications. Applied Clay Science, 177, 91-113.

Liu, W., Xu, X., Wu, X., Yang, Q., Luo, Y., and Christie, P. (2006) Decomposition of silicate minerals by Bacillus mucilaginosus in liquid culture. Environmental Geochemistry and Health, 28(1), 133-140.

Malinovskaya, I.M., Kosenko, L.V., Votselko, S.K., and Podgorskii, V.S. (1990) Role of Bacillus mucilaginosus polysaccharide in degradation of silicate minerals. Microbiology, 59(1), 49-55.

Manceau, A., Lanson, B., Drits, V.A., Chateigner, D., Gates, W.P., Wu, J., ... and Stucki, J.W. (2000) Oxidation-reduction mechanism of iron in dioctahedral smectites: I. Crystal chemistry of oxidized reference nontronites. American Mineralogist, 85(1), 133-152.

McCafferty, E.W.J.P., and Wightman, J.P. (1998) Determination of the concentration of surface hydroxyl groups on metal oxide films by a quantitative XPS method. Surface and Interface Analysis, 26(8), 549-564.

Mo, B., and Lian, B. (2011) Interactions between Bacillus mucilaginosus and silicate minerals (weathered adamellite and feldspar): Weathering rate, products, and reaction mechanisms. Chinese Journal of Geochemistry, 30(2), 187-192.

Mueller, B. (2015) Experimental interactions between clay minerals and bacteria: a review. Pedosphere, 25(6), 799-810.

Rajawat, M. V. S., Singh, R., Singh, D., Yadav, A. N., Singh, S., Kumar, M., & Saxena, A.

K. (2020). Spatial distribution and identification of bacteria in stressed environments capable to weather potassium aluminosilicate mineral. Brazilian Journal of Microbiology, 51(2), 751-764.

Robert, C., and Kennett, J.P. (1992) Paleocene and Eocene kaolinite distribution in the South Atlantic and Southern Ocean: Antarctic climatic and paleoceanographic implications. Marine Geology, 103(1-3), 99-110.

Ryan P.C. and Huertas F.J. (2013) Reaction Pathways of Clay Minerals in Tropical Soils: Insights from Kaolinite-smectite Synthesis Experiments. Clays and Clay Minerals, 61(4), 303-318.

Ryan P.C. and Huertas F.J. (2009) The temporal evolution of pedogenic Fe–smectite to Fe–kaolin via interstratified kaolin–smectite in a moist tropical soil chronosequence. Geoderma, 151(1), 1-15.

Shelobolina, E.S., Konishi, H., Xu, H., Benzine, J., Xiong, M.Y., Wu, T., ... and Roden, E. (2012) Isolation of phyllosilicate–iron redox cycling microorganisms from an illite–smectite rich hydromorphic soil. Frontiers in microbiology, 3, 134.

Ulagappan, N., and Frei, H. (2000) Mechanistic study of CO_2 photoreduction in Ti silicalite molecular sieve by FT-IR spectroscopy. The Journal of Physical Chemistry A, 104(33), 7834-7839.

Welch, S. A., & Ullman, W. J. (1996). Feldspar dissolution in acidic and organic solutions: Compositional and pH dependence of dissolution rate. Geochimica et Cosmochimica Acta, 60(16), 2939-2948.

White, G.N. and Zelazny, L.W. (1988) Analysis and implications of the edge structure of dioctahedral phyllosilicates. Clays and Clay Minerals, 36, 141–146

Wollast, R. (1967). Kinetics of the alteration of K-feldspar in buffered solutions at low temperature. Geochimica et Cosmochimica Acta, 31(4), 635-648.

Xiao, L., Hao, J., Wang, W., Lian, B., Shang, G., Yang, Y., ... and Wang, S. (2014) The up-regulation of carbonic anhydrase genes of Bacillus mucilaginosus under soluble Ca^{2+} deficiency and the heterologously expressed enzyme promotes calcite dissolution. Geomicrobiology Journal, 31(7), 632-641.

Yang, X., Li, Y., Lu, A., Wang, H., Zhu, Y., Ding, H., and Wang, X. (2016) Effect of Bacillus mucilaginosus D4B1 on the structure and soil-conservation-related properties of montmorillonite. Applied Clay Science, 119, 141-145.

Zhang, C., Guo, Z., Deng, C., Ji, X., Wu, H., Paterson, G. A., ... and Zhu, R. (2016) Clay mineralogy indicates a mildly warm and humid living environment for the Miocene hominoid from the Zhaotong Basin, Yunnan, China. Scientific reports, 6(1), 1-10.

Zhao, L., Dong, H., Edelmann, R.E., Zeng, Q., and Agrawal, A. (2017) Coupling of Fe(II) oxidation in illite with nitrate reduction and its role in clay mineral transformation. Geochimica et Cosmochimica Acta, 200, 353-366.

Zor, T., and Selinger, Z. (1996) Linearization of the Bradford protein assay increases its sensitivity: theoretical and experimental studies. Analytical biochemistry, 236(2), 302-308.

Figure captions

Fig. 1 Changes in pH and produced protein (a), concentration of Si and Al (b) in three experiment systems.

Fig. 2 Morphology images of final solid products from experiments with heat-inactivated cells (a) and living cells (b, c). Black arrow in b points out the bacterium. Inset of c: EDS and SAED patterns of amorphous particles in c.

Fig. 3 The Si *2p* (a), Al *2p* (b), Mg *2p* (c), Ca *2p* (d) and Fe *2p* (e) core-level XPS in two final 25-day solid products obtained in living-cell system and abiotic control.

Fig. 4 XRD patterns of solid products on 5, 10 and 25 day (λ=0.12398 nm). "Sme" and "Kln" are abbreviations of smectite and kaolinite, respectively.

Fig. 5 Lattice fringe images and EDS patterns of two final solid products obtained in heat-inactivated cells system (a-c) and living-cell system (d-i).

Fig. 6 Structure models of a smectite-kaolinite mixed-layer and corresponding HRTEM images.

Fig. 7 Organic acid identification by Micro-FTIR spectroscopy in middle-infrared band (a-b) and C 1s core-level X-ray photoelectron spectroscopy after 25 days (c-d).

Fig. 8 Potential reaction mechanisms of smectite layers to kaolin layers by *B. mucilaginosus*. Smectite 2:1 layers and kaolin 1:1 layers are denoted by "Sme" and "Kln", respectively.

Tables

Table 1 XPS peak area ratio of detected atoms on smectite in living cells system (SBM) and the blank group (SC).

Peak area ratio	Si/Al	Si/Mg	Si/Ca	Si/Fe
SC	7.59	42.09	4.32	2.29
SBM	6.51	37.12	3.55	1.98

This is the peer-reviewed, final accepted version for American Mineralogist, published by the Mineralogical Society of America.
The published version is subject to change. Cite as Authors (Year) Title. American Mineralogist, in press.
DOI: https://doi.org/10.2138/am-2022-8442. http://www.minsocam.org/

Figures

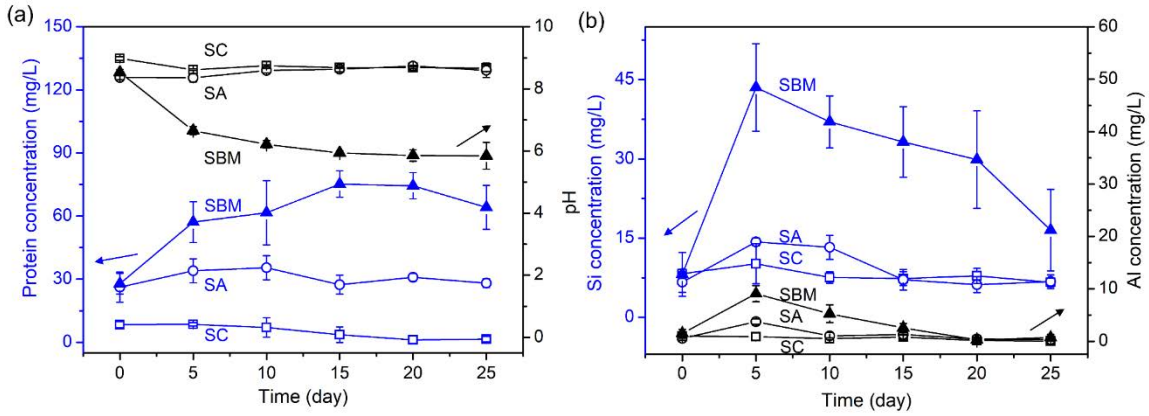

Fig. 1 Changes in pH and produced protein (a), concentration of Si and Al (b) in three experiment systems.

This is the peer-reviewed, final accepted version for American Mineralogist, published by the Mineralogical Society of America.
The published version is subject to change. Cite as Authors (Year) Title. American Mineralogist, in press.
DOI: https://doi.org/10.2138/am-2022-8442. http://www.minsocam.org/

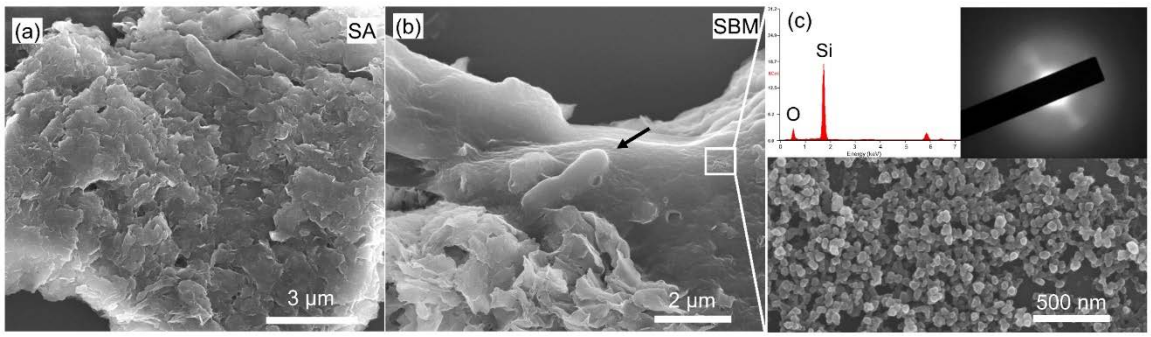

Fig. 2 Morphology images of final solid products from experiments with heat-inactivated cells (a) and living cells (b, c). Black arrow in b points out the bacterium. Inset of c: EDS and SAED patterns of amorphous particles in c.

This is the peer-reviewed, final accepted version for American Mineralogist, published by the Mineralogical Society of America.
The published version is subject to change. Cite as Authors (Year) Title. American Mineralogist, in press.
DOI: https://doi.org/10.2138/am-2022-8442. http://www.minsocam.org/

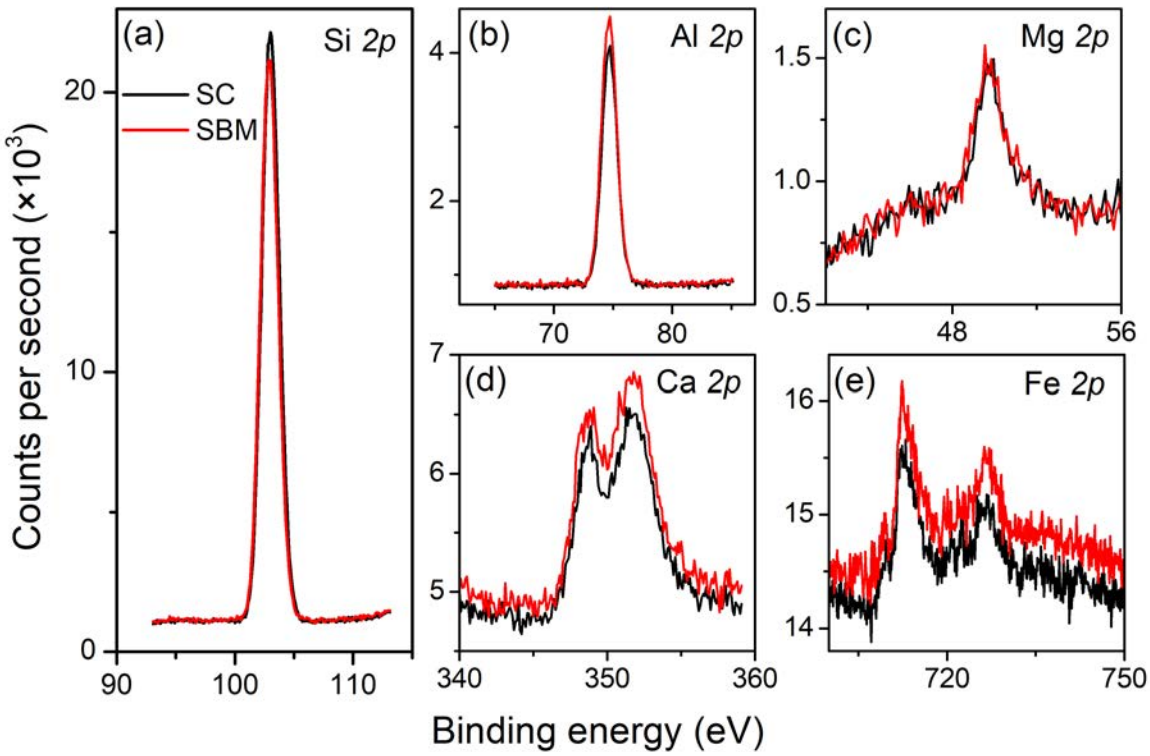

Fig. 3 The Si *2p* (a), Al *2p* (b), Mg *2p* (c), Ca *2p* (d) and Fe *2p* (e) core-level XPS in two final 25-day solid products obtained in living-cell system and abiotic control.

This is the peer-reviewed, final accepted version for American Mineralogist, published by the Mineralogical Society of America.
The published version is subject to change. Cite as Authors (Year) Title. American Mineralogist, in press.
DOI: https://doi.org/10.2138/am-2022-8442. http://www.minsocam.org/

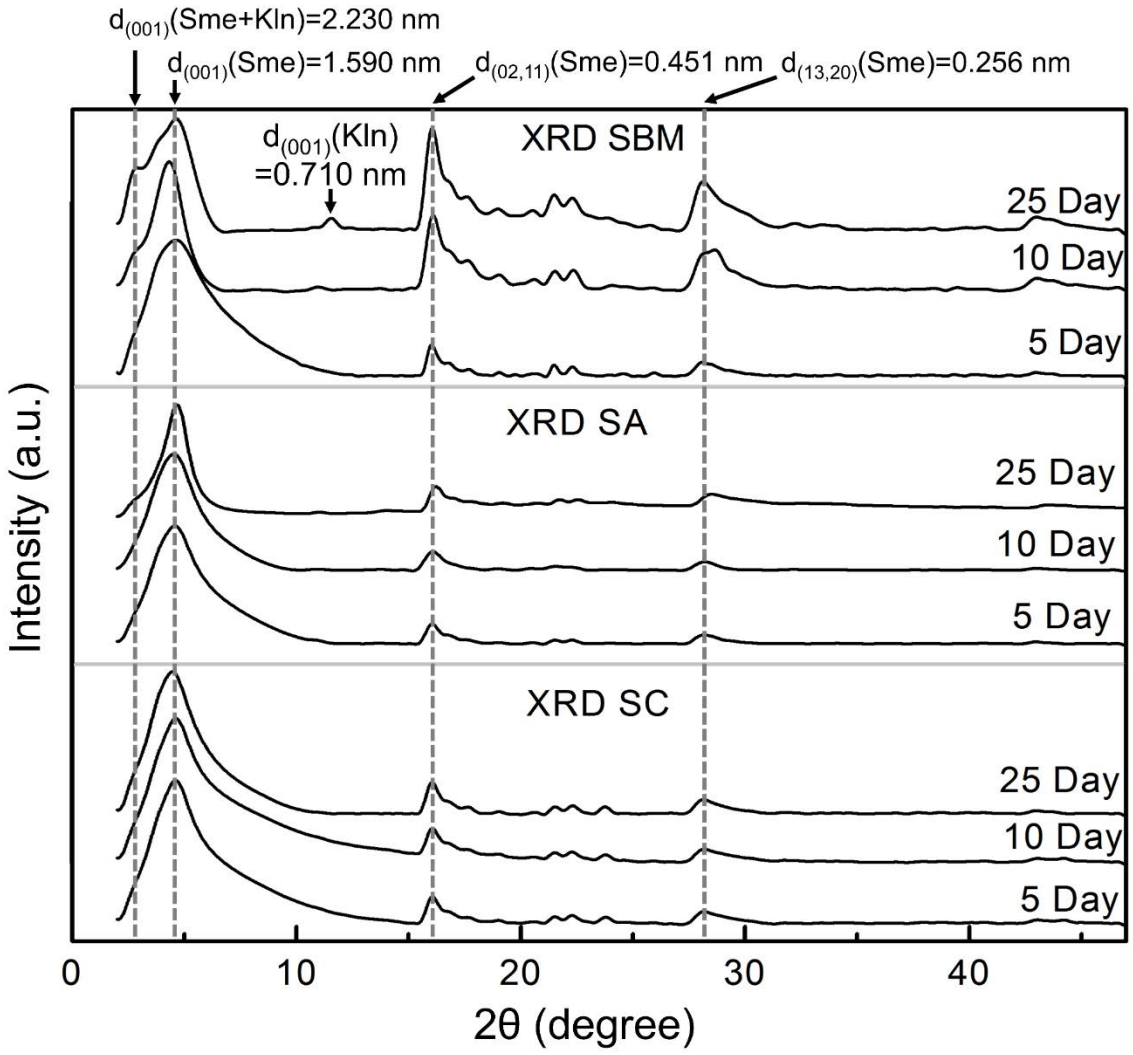

Fig. 4 XRD patterns of solid products on 5, 10 and 25 day (λ=0.12398 nm). "Sme" and "Kln" are abbreviations of smectite and kaolinite, respectively.

This is the peer-reviewed, final accepted version for American Mineralogist, published by the Mineralogical Society of America.
The published version is subject to change. Cite as Authors (Year) Title. American Mineralogist, in press.
DOI: https://doi.org/10.2138/am-2022-8442. http://www.minsocam.org/

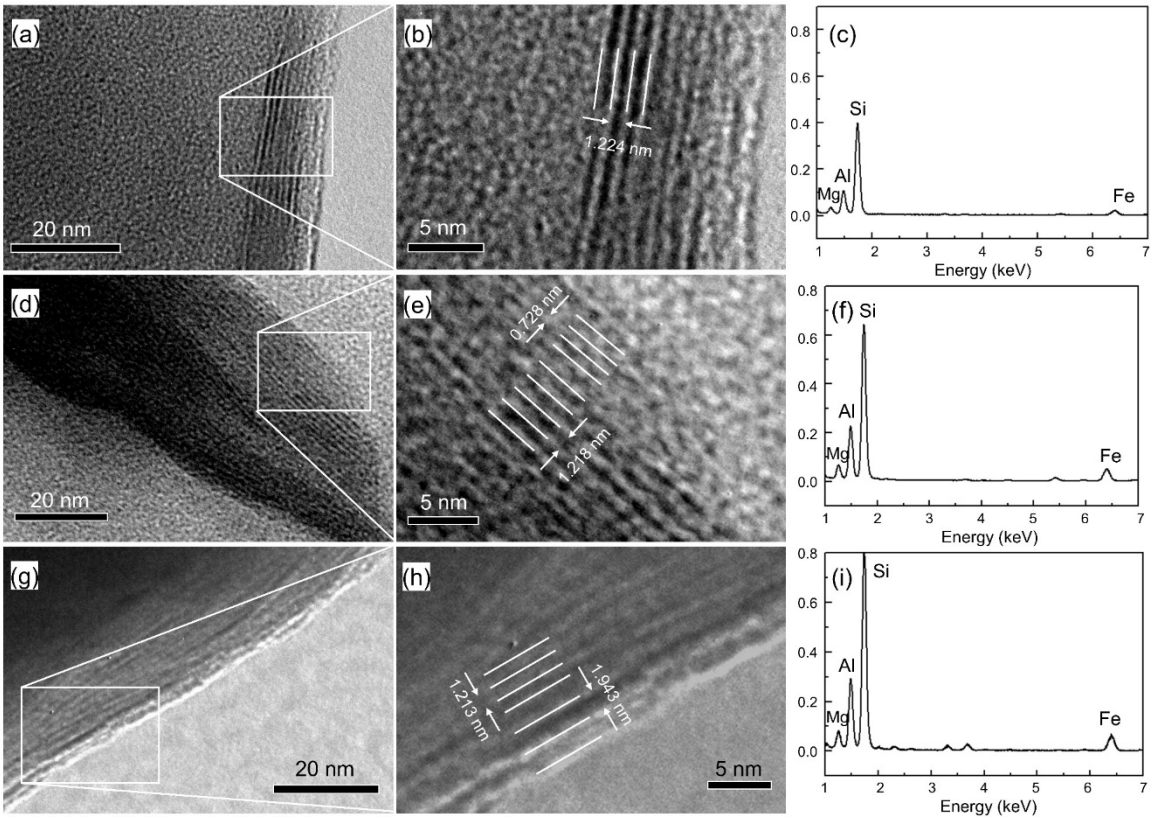

Fig. 5 Lattice fringe images and EDS patterns of two final solid products obtained in heat-inactivated cells system (a-c) and living-cell system (d-i).

This is the peer-reviewed, final accepted version for American Mineralogist, published by the Mineralogical Society of America.
The published version is subject to change. Cite as Authors (Year) Title. American Mineralogist, in press.
DOI: https://doi.org/10.2138/am-2022-8442. http://www.minsocam.org/

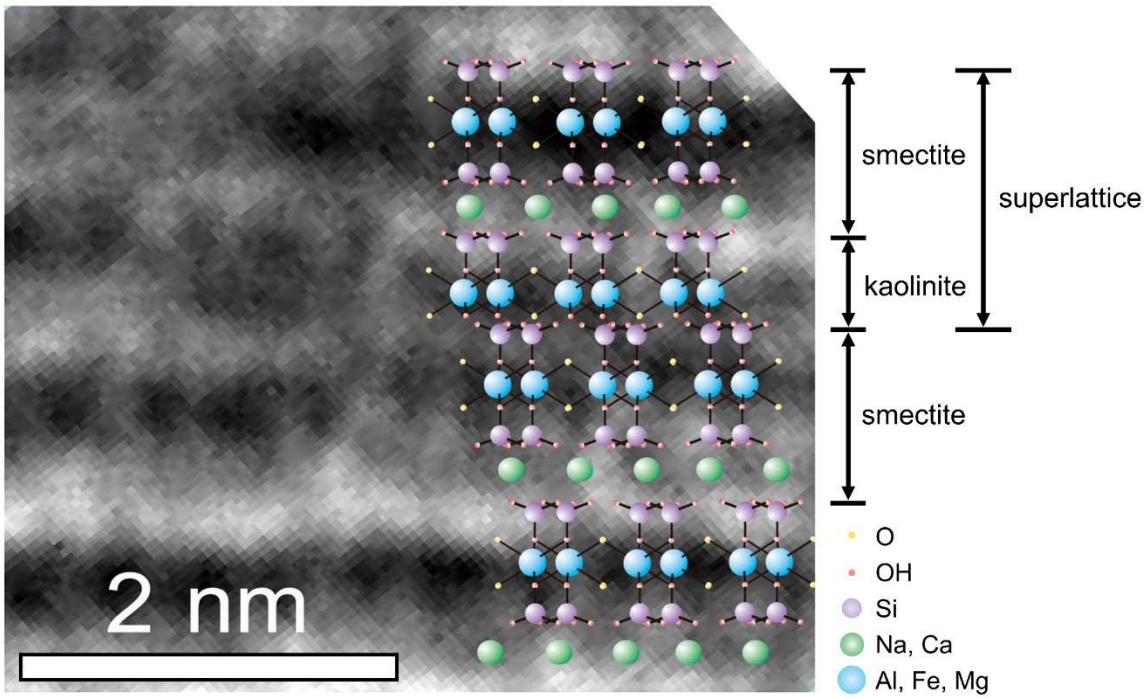

Fig. 6 Structure models of a smectite-kaolinite mixed-layer and corresponding HRTEM images.

This is the peer-reviewed, final accepted version for American Mineralogist, published by the Mineralogical Society of America.
The published version is subject to change. Cite as Authors (Year) Title. American Mineralogist, in press.
DOI: https://doi.org/10.2138/am-2022-8442. http://www.minsocam.org/

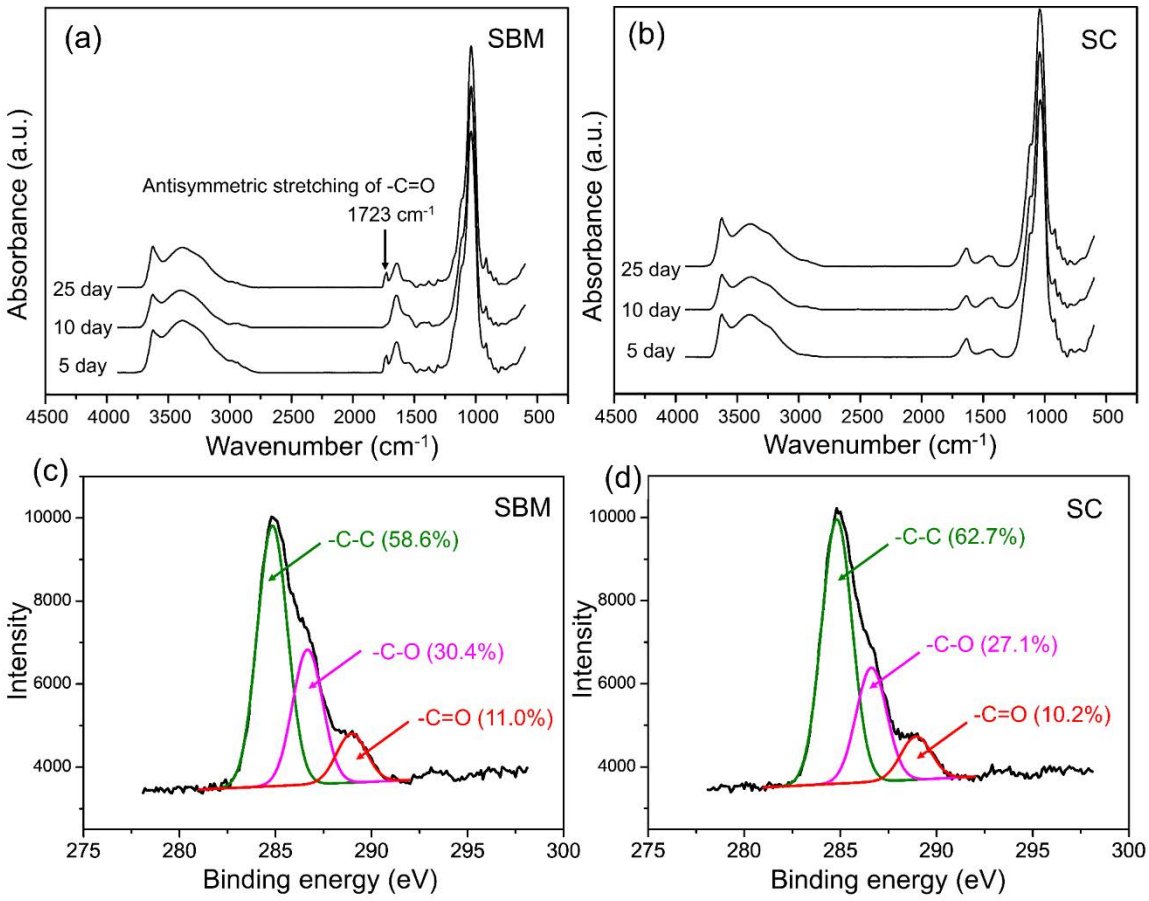

Fig. 7 Organic acid identification by Micro-FTIR spectroscopy in middle-infrared band (a-b) and C 1s core-level X-ray photoelectron spectroscopy after 25 days (c-d).

This is the peer-reviewed, final accepted version for American Mineralogist, published by the Mineralogical Society of America.
The published version is subject to change. Cite as Authors (Year) Title. American Mineralogist, in press.
DOI: https://doi.org/10.2138/am-2022-8442. http://www.minsocam.org/

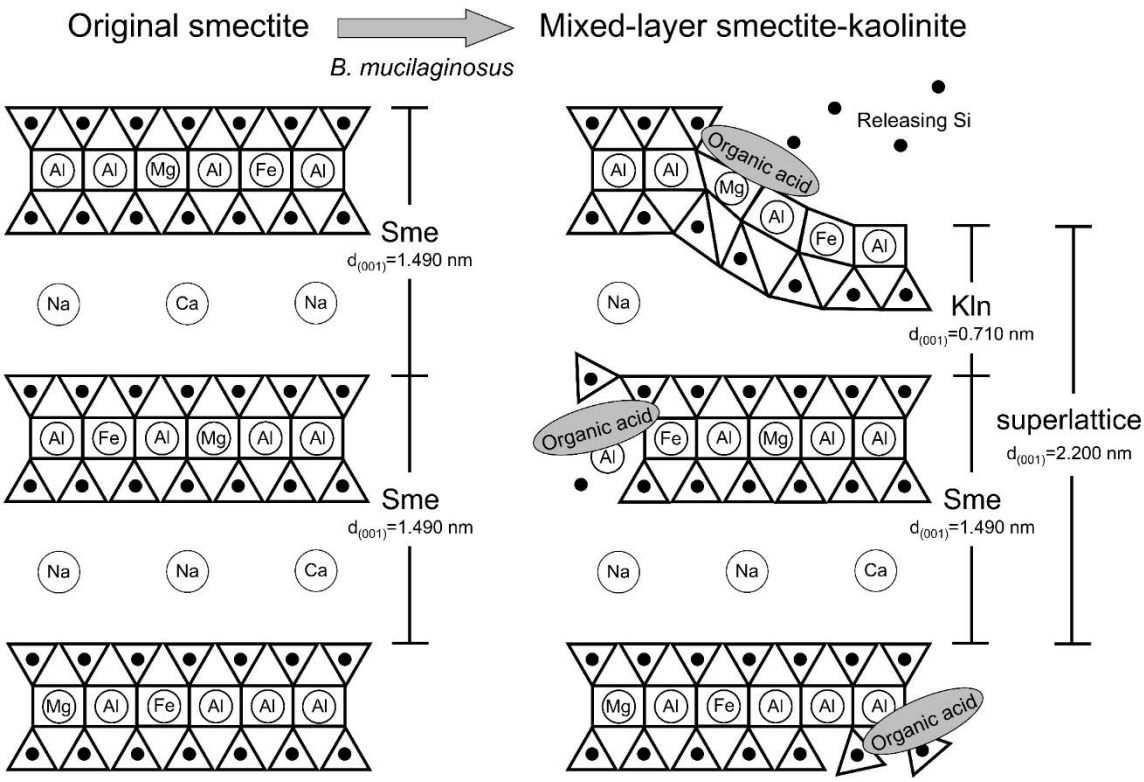

Fig. 8 Potential reaction mechanisms of smectite layers to kaolin layers by *B. mucilaginosus*. Smectite 2:1 layers and kaolin 1:1 layers are denoted by "Sme" and "Kln", respectively.